Available online at www.sciencedirect.com

ScienceDirect

Journal of Magnesium and Alloys 10 (2022) 3418–3432

www.elsevier.com/locate/jma

Full Length Article

In-situ observation of twinning and detwinning in AZ31 alloy

Wu Gong[a,b,*], Ruixiao Zheng[c,d,**], Stefanus Harjo[a], Takuro Kawasaki[a], Kazuya Aizawa[a], Nobuhiro Tsuji[b,c]

[a] *J-PARC Center, Japan Atomic Energy Agency, 2-4 Shirane Shirakata, Tokai, Naka, Ibaraki 319-1195, Japan*
[b] *Center for Elements Strategy Initiative for Structural Materials, Kyoto University, Yoshidahonmachi, Sakyo-ku, Kyoto 606-8501, Japan*
[c] *Department of Materials Science and Engineering, Kyoto University, Yoshida-honmachi, Sakyo-ku, Kyoto 606-8501, Japan*
[d] *School of Materials Science and Engineering, Beihang University, Beijing 100191, China*

Received 2 November 2021; received in revised form 7 January 2022; accepted 6 February 2022
Available online 11 March 2022

Abstract

Twinning and detwinning behavior of a commercial AZ31 magnesium alloy during cyclic compression–tension deformation with a total strain amplitude of 4% (±2%) was evaluated using the complementary techniques of *in-situ* neutron diffraction, identical area electron backscatter diffraction, and transmission electron microscopy. *In-situ* neutron diffraction demonstrates that the compressive deformation was dominated by twin nucleation, twin growth, and basal slip, while detwinning dominated the unloading of compressive stresses and subsequent tension stage. With increasing number of cycles from one to eight: the volume fraction of twins at -2% strain gradually increased from 26.3% to 43.5%; the residual twins were present after 2% tension stage and their volume fraction increased from zero to 3.7% as well as a significant increase in their number; and the twinning spread from coarse grains to fine grains involving more grains for twinning. The increase in volume fraction and number of residual twins led to a transition from twin nucleation to twin growth, resulting in a decrease in yield strength of compression deformation with increasing cycles. A large number of <c>-component dislocations observed in twins and the detwinned regions were attributed to the dislocation transmutation during the twinning and detwinning. The accumulation of barriers including twin boundaries and various types of dislocations enhanced the interactions of migrating twin boundary with these barriers during twinning and detwinning, which is considered to be the origin for increasing the work hardening rate in cyclic deformation of the AZ31 alloy.

Keywords: Magnesium; Neutron diffraction; Twinning; Detwinning; Dislocation transmutation.

1. Introduction

Basal slip and $\{10\bar{1}2\}$ twinning are well known to be the basic deformation modes in magnesium (Mg) and its alloys. Basal slip is the principal deformation mode, however, it cannot accommodate the strain along the *c*-axis. $\{10\bar{1}2\}$ twinning, the so-called tension twinning or extension twinning, whose critical resolved shear stress (CRSS) is slightly higher than the basal slip [1,2], can accommodate the tensile strains along the *c*-axis. Therefore, $\{10\bar{1}2\}$ twinning is considered to be a key factor in improving the ductility of Mg alloys [1–3]. $\{10\bar{1}2\}$ twinning can be readily activated in the grains subjected to a tensile stress parallel to the *c*-axis [3] or a compressive stress perpendicular to the *c*-axis [3,4], but is absent in the opposite stress state. This polar feature of deformation twinning is the reason for the high plastic anisotropy in Mg and its alloys, especially in wrought conditions because of the texture [3–8]. Another important feature of $\{10\bar{1}2\}$ twinning is its reversibility, in which the orientation of deformation twins can revert to the initial orientation by reversing the applied stress

* Corresponding author at: J-PARC Center, Japan Atomic Energy Agency, 2-4 Shirane Shirakata, Tokai, Naka, Ibaraki 319-1195, Japan.
** Corresponding author at: School of Materials Science and Engineering, Beihang University, Beijing 100191, China.
E-mail addresses: gong.wu@jaea.go.jp (W. Gong), zhengruixiao@buaa.edu.cn (R. Zheng).

https://doi.org/10.1016/j.jma.2022.02.002

[4,8–12] or even a reversal of internal stress during unloading [13–15], which is known as detwinning (or untwinning). Because of the reversible feature, twinning and detwinning have been confirmed as the main plastic deformation modes in a variety of Mg alloys including pure Mg [8], Mg-7.7Al (at.%) [14], AZ31 [4,9,12], ZK60 [10,11], and AZ91 [8], when the specimens were subjected to alternate loading conditions, such as cyclic deformations with compression–tension [4,9–11], tension–compression [4], or loading–unloading [13–15].

In general, work hardening in plastic deformation of structural metallic materials is caused by the interactions between plastic deformation and barriers such as grain boundary [16–20], dislocations [21,22], and second-phase particles [14]. Moreover, plastic deformation generally introduces various barriers in the microstructure, including dislocations, phase boundaries (i.e., transformation-induced plasticity [23]), and twinning boundaries (TBs) [18,24–26], which are important strengthening mechanisms in the development of structural metallic materials. It has been reported that the TBs as the coherent boundaries with low excess energies contribute strength through interaction with dislocation motion and increase ductility through creating local sites for nucleating and accommodating dislocations [18,24,26]. The TBs in Mg alloys are movable through twin growth or twin shrinkage, i.e., detwinning [8,25]. The pinning effect of TBs by the segregation of solute atoms can increase the strength of Mg alloys [25]. Similarly, the motion of TBs can be suppressed by dislocations introduced by pre-strains, leading to changes in morphology of twins and the stress-strain response [27–30]. Actually, dislocations are allowed to penetrate the TBs [2,31–34]. Therefore, the interactions between dislocations and TBs, and the feature of dislocations after penetration of TBs are a concern for the mechanical properties. A dislocation transmutation has been reported in interactions between dislocations and TBs based on the experimental evidence, where the dislocations with Burgers vector of <a> were found to transmute into <a> or <c + a> after penetration of TBs [33,35]. More recently, I_1 stacking faults, lying on the basal planes of twins, have been observed, and were considered to be associated with the glissile-to-sessile transition during twinning [36,37]. The reaction between dislocations and TBs would establish a basis for work hardening during twinning deformation [38]. Moreover, the hardening of twins by the increase in dislocation multiplicity (i.e., dislocation type) within twins was reported through simulations by Kadiri and Opeddal [31] and Oppedal et al. [32]. These studies mainly focused on the interaction between dislocations and motion of TBs during twinning, whereas in the detwinning process the effect of these interactions on the mechanical properties are still far from being understood. Therefore, to track the evolutions of twins and dislocation structures during cyclic deformation in Mg alloys is crucial for understanding the mechanical properties.

Because of the unique crystallographic feature, twinning and detwinning behavior matches well with the information provided by diffraction techniques, such as electron backscatter diffraction (EBSD) and neutron diffraction (ND). Both techniques have their respective advantages. *In-situ* ND provides the bulk averaged crystallographic information such as volume fraction of twins [10,13,14,39] and lattice strain [11,13,14,39,40] for interpretation of macroscopic deformation behavior. Conversely, EBSD provides information focusing on local details such as area fraction of twins [8,12,27–29], morphology [12,27,27–29], variant selection [8,12,41], and crystallographic features of various boundaries [8,41,42]. The obtained EBSD results can be used to interpret the work hardening behavior with respect to grain size dependence [12], orientation dependence [43], and boundary feature dependence [8,41] of twinning. Although great efforts have been made on the deformation mechanisms of low cycle fatigue properties in Mg and alloys, the relationship between the deformation mechanisms and the mechanical responses is yet to be fully understood.

In the present study, the deformation mechanisms with respect to twinning, detwinning, and their interaction with dislocations during compression–tension cyclic deformation in a commercial AZ31 Mg alloy were evaluated systematically using a combination of *in-situ* ND, identical area EBSD, and transmission electron microscopy (TEM) techniques. The mechanical responses in compression–tension cyclic deformation are discussed with bulk averaged twin volume fraction (TVF), the local details of twinned microstructure, and the dislocation structures.

2. Experimental methods

2.1. In-situ neutron diffraction

Commercial AZ31 alloy (Mg-3 wt.%Al-1 wt.%Zn) extruded rods with a diameter of 52 mm were used in this study. The rods were extruded at 623 K with an extrusion ratio of 9. Cylindrical tensile specimens with a gage diameter of 6 mm and a length of 17 mm were cut from the as-extruded rod for *in-situ* ND experiment. The loading direction was parallel to the extrusion direction (ED). The *in-situ* ND experiment during deformation was performed using a time-of-flight (TOF) engineering neutron diffractometer "TAKUMI" at the Japan Proton Accelerator Research Complex (J-PARC) Fig. 1a shows the geometrical arrangement of the *in-situ* ND experiment. The specimen was set up on the loading frame horizontally, with its loading axis angled −45° relative to the incident neutron beam. TAKUMI has two detector banks, south bank and north bank, positioned at +90° and −90° relative to the incident beam. As a result, the diffraction vectors observed by the south and north banks were parallel to the loading direction (hereafter, labeled as LD//) and perpendicular to the loading direction (hereafter, labeled as LD⊥), respectively. The incident beam was set as 5 mm in width and 5 mm in height. A combination of the incident beam size and 5 mm-width radial collimators placed in front of the detector banks defined that a 5 mm cubic located at the gage center of the specimen was measured. The neutron wavelength range of 0.094–0.471 nm (i.e., d-range

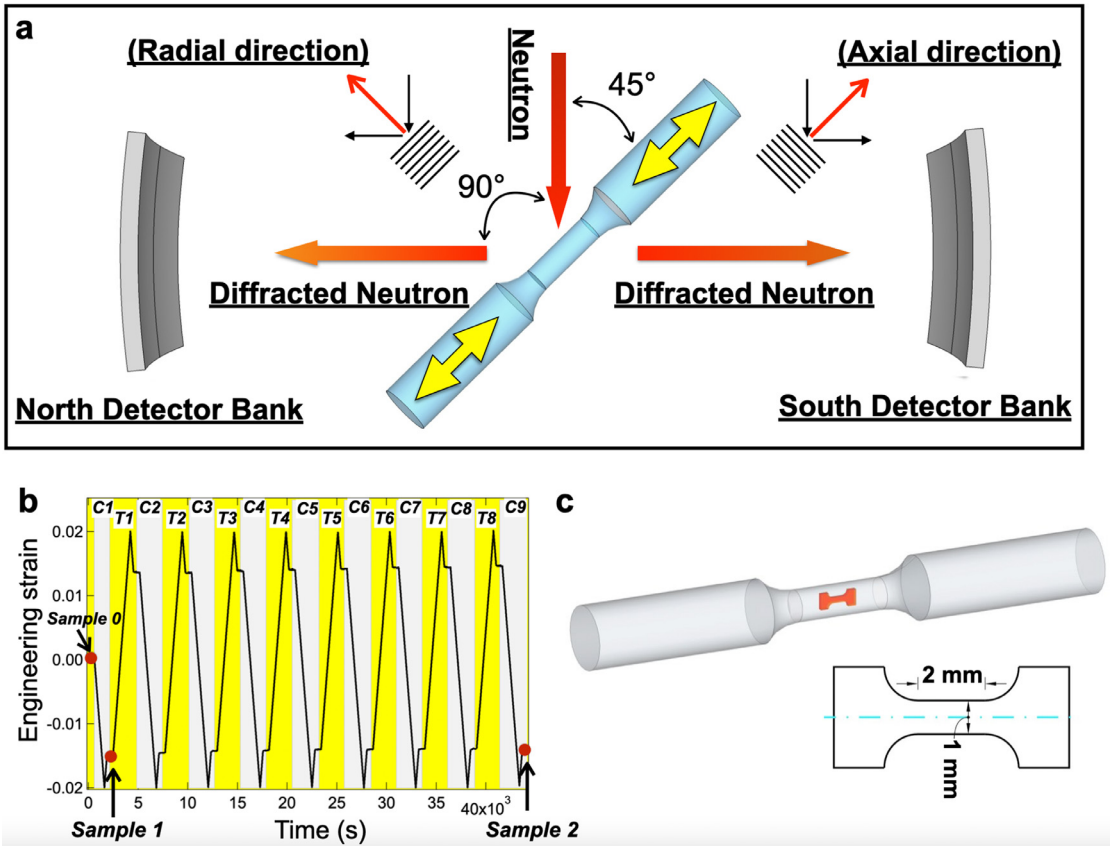

Fig. 1. Multiscale experimental methods. (a) Diffraction geometry of the *in-situ* neutron diffraction experimental arrangements, (b) sequence of the cyclic compression–tension deformation applied to the AZ31 alloy. *Ci* and *Ti* represent the compression and tension steps of the *i*th cycle, and (c) schematic showing the dog-bone-shaped specimen for electron backscatter diffraction analysis cut from prestrained cylindrical tensile specimens (For interpretation of the references to color in this figure, the reader is referred to the web version of this article).

of 0.067–0.333 nm) was selected for the present experiment. Details of the diffractometer have been described elsewhere [44].

Fully reversed strain-controlled cyclic compression–tension deformation with a total strain amplitude of 4% (± 2%) at a strain rate of 2×10^{-5} s^{-1} was applied to the cylindrical tensile specimens. All steps of the cyclic deformation were conducted with strain control through the strain gage attached to the specimen. The KFEM series strain gages (Kyowa Electronic Instruments Co. Ltd.) having a strain limit of 20% were used Fig. 1.b shows the sequence of cyclic deformation. After each unloading step, an interruption of 10 min was set for collecting more statistics of diffraction profile. Eight cycles were performed for the *in-situ* ND experiment. After the *in-situ* ND experiment, an additional compression to −2% strain was performed on the specimen as to be the initial condition for the identical area EBSD observation. As marked in Fig. 1b, hereafter, the compression and tension steps of the *i*th cycle are denoted as *Ci* and *Ti*, respectively.

Diffraction profiles were analyzed using the Z-Rietveld code to obtain integrated intensities of selected diffraction reflections via a single-peak fitting procedure [45]. Evolution of the TVF was analyzed using the Material Analysis Using Diffraction program [46] combined with the MTEX program [47]; the details are described elsewhere [39].

2.2. Identical area electron backscatter diffraction observation

Two cylindrical tensile specimens, *Sample 1* and *Sample 2* (marked as red dots in Fig. 1b), were prepared according to the following procedures. *Sample 1* was compressed to −2% strain from the initial condition (i.e., *C1*), and *Sample 2* was compressed to −2% strain after eight cycles of compression–tension with ±2% (i.e., *C9*). As illustrated in Fig. 1c, a small dog-bone-shaped specimen with a gage length of 2 mm and a gage cross section of 1 × 0.5 mm was cut from the prestrained specimen for EBSD analyses. The specimens for EBSD analysis were mechanically polished using a fine grade sandpaper followed by a final polish using a colloidal silica suspension (OP-S, Struers). The microstructures were characterized using a TSL EBSD system equipped on a JEOL JSM-7100F scanning electron microscope (SEM). The EBSD analyses at the identical areas were performed on samples after providing step-by-step tension to various strains. Tensile tests were conducted using a Shimadzu tensile testing machine at ambient temperature outside of SEM equip-

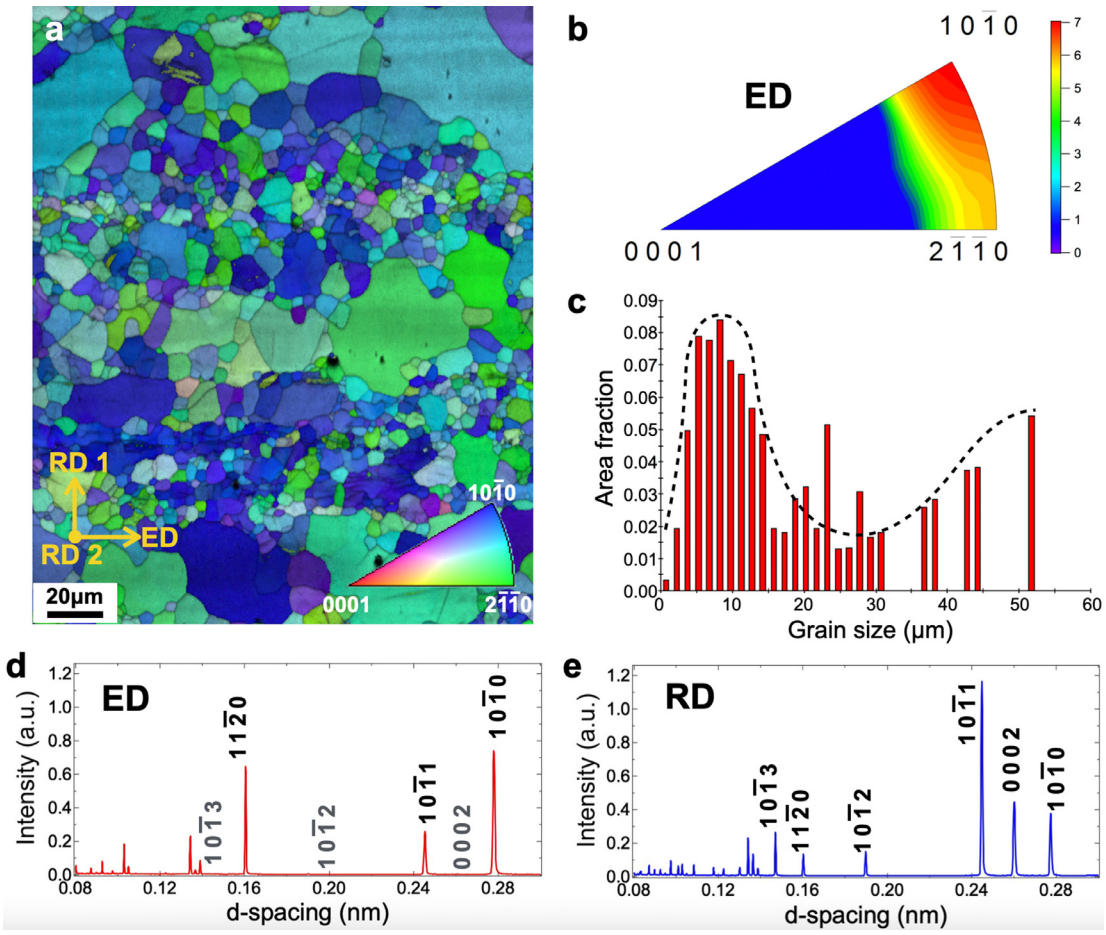

Fig. 2. Initial microstructure. (a) Inverse pole figure (IPF) map of the cross section of the extruded AZ31 magnesium alloy, (b) corresponding IPF showing initial basal texture (standard stereographic triangle showing extrusion direction), and (c) related bimodal grain size distribution. The initial diffraction profiles of (d) axial (extrusion) and (e) radial directions.

ment. The EBSD data were postprocessed using the commercial TSL OIM analysis software.

2.3. Transmission electron microscopy measurement

The foil specimens for TEM observation were cut from the aforementioned cylindrical tensile specimen along the longitudinal section. TEM specimens were prepared by mechanical grinding, followed by twin-jet electropolishing. TEM characterization of microstructure was conducted using a JEOL JEM-2010 and was operated at 200 kV.

3. Results

3.1. Initial microstructure characteristics

The microstructure characteristics of the as-received extruded AZ31 alloy sample (denoted by *Sample 0*) are shown in Fig. 2. The inverse pole figure (IPF) map in Fig. 2a was observed on the longitudinal section of the extruded rod, in which the colors correspond to the crystallographic orientations parallel to the ED. The IPF map and IPF (Fig. 2b) of the ED demonstrate a typical basal texture generated by extrusion, i.e., *c*-axes perpendicular to the ED [8,9,12,48]. As shown in the grain size distribution chart in Fig. 2c, the IPF map shows a twin-free and bimodal grain structure, which consists of fine and coarse equiaxed grains with average grain size of 11.7 μm and 40.2 μm, respectively. The average grain size of all grains is approximately 18 μm. Bimodal microstructures consisting of fine and relatively coarse DRXed grains have been frequently observed in magnesium alloys subjected to extrusion at relatively low temperatures [49,50], which are related to the pinning of grain boundary by precipitates and also the sequence of precipitation and recrystallization [51]. The extrusion parameters of the present material may be in the critical region for forming the bimodal grain structure.

The ND profiles of the initial condition in LD// (Fig. 2d) and LD⊥ (Fig. 2e) exhibit different intensities. The {*hkil*} lattice planes close to the basal plane such as {0002}, {10$\bar{1}$2}, and {10$\bar{1}$3} were absent in the LD// diffraction pattern, whereas they were intense in the LD⊥ pattern. The ND patterns show an initial texture consistent with that obtained by the EBSD analysis.

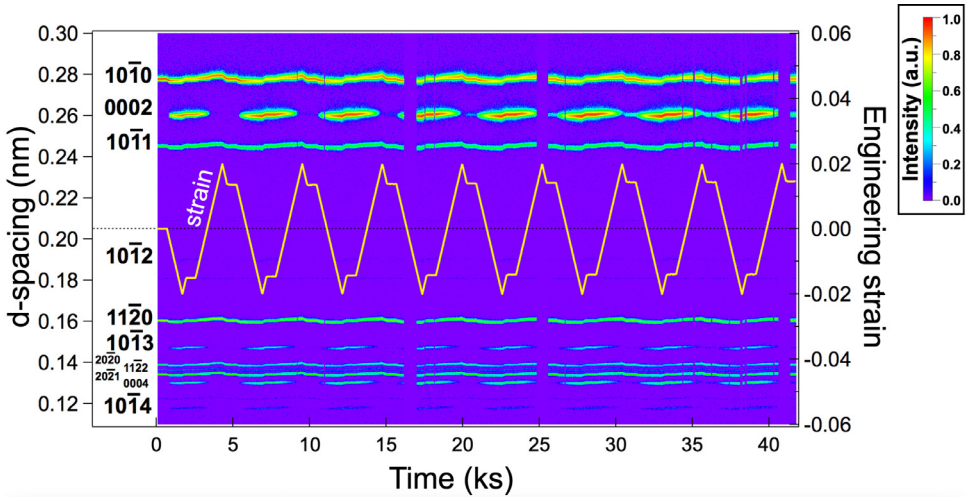

Fig. 3. Twinning and detwinning behavior during cyclic deformation tracked using *in-situ* neutron diffraction (ND). Evolution of ND profiles along an axial direction corresponding to the cyclic compression–tension test, which shows alternate changes of diffraction reflections. Change in macroscopic strain was superimposed for reference.

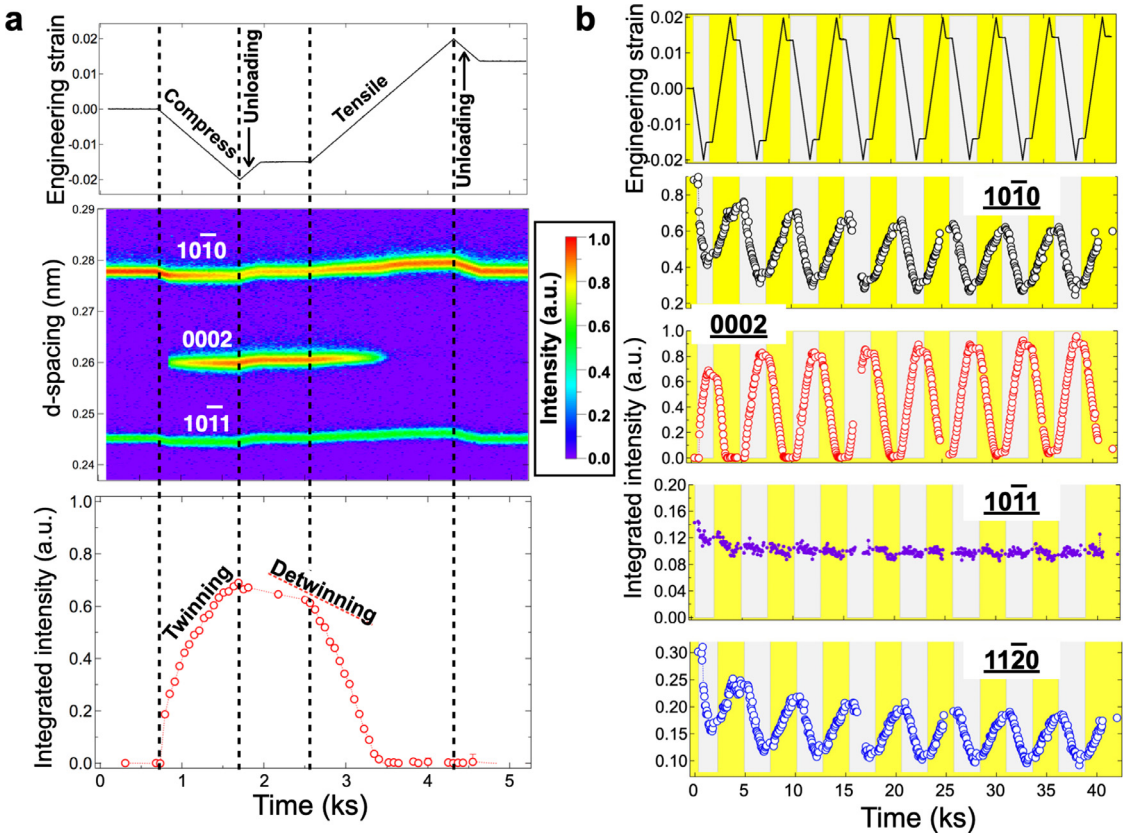

Fig. 4. (a) Detailed changes of the macroscopic strain, diffraction profiles, and integrated intensity of the 0002 diffraction reflection along the axial direction in cycle 1 showing the twinning and detwinning behavior directly and (b) evolutions of the integrated intensities of representative *hkil* diffraction reflections along the axial direction during cycle compression–tension deformation.

3.2. Twinning and detwinning behavior tracked by in-situ *neutron diffraction*

Using a pulsed neutron source and the TOF diffraction method, a wide range of wavelengths can be used to detect various {*hkil*} lattice planes simultaneously Fig. 3 shows the evolution of the ND patterns along LD// corresponding to the cyclic compression–tension test. Note that several lines at around 17, 25, and 41 ks showing no intensity were caused by the accidental stop of beam. As mentioned above, initial extrusion texture led to the absence of Bragg reflections such as {0002}, {$10\bar{1}3$}, and {$10\bar{1}4$} before deformation. In the sub-

sequent deformation, the evolution of the diffraction pattern shows alternate increase and decrease in the aforementioned absent Bragg reflections corresponding to the cyclic loading.

Fig. 4a demonstrates the detailed changes of the diffraction patterns in cycle 1. The intensities of the $\{10\bar{1}0\}$ reflection decreased accompanied with an increase in the $\{0002\}$ reflection in compression, while the tendency changed conversely during unloading after compression and in the subsequent tensile deformation. It coincides with the lattice reorientation by $\{10\bar{1}2\}$ twinning and detwinning in Mg and its alloys [10,11,13]. Under the present initial texture, compressive loading parallel to ED promoted $\{10\bar{1}2\}$ twinning but was unfavorable for basal slip. In subsequent tension after compression, tensile stress applied on the *c*-axis of twins favored the activation of detwinning. A slight decrease in the integrated intensity of the $\{0002\}$ reflection also appeared during unloading after compression, which shows the occurrence of detwinning (see bottom graph in Fig. 4a). The intergranular stress was considered as the origin of detwinning [11,13].

Evolutions of the integrated intensity of representative $\{hkil\}$ Bragg reflections along LD// are compared in Fig. 4b. The grains with $\{10\bar{1}0\}$ and $\{11\bar{2}0\}$ Bragg reflections whose integrated intensities decreased during twinning and partially reversed during detwinning, were defined as "matrix." In contrast, the grains with $\{0002\}$ Bragg reflection (together with $\{10\bar{1}3\}$ and $\{10\bar{1}4\}$ Bragg reflections) that exhibited the opposite tendency of integrated intensity change were defined as "twins." The integrated intensity for grains with $\{10\bar{1}1\}$ Bragg reflection showed less variation, which shows that twinning was unfavorable in them, but is known to be dominated by basal slip [11,13].

The axial distribution function (ADF) of the basal pole has been proved to be reliable for determining the TVF in Mg alloys having axisymmetric texture [7,39,48,52]. The ADF of the basal pole at unloading conditions of each step is plotted in Fig. 5a. The 0° and 90° of the horizontal axis represent that the *c*-axes of the grains are parallel and perpendicular to the loading direction, respectively. As seen, the intensity of the basal pole distributed around 0° after compression is evidently higher than that after tension, and gradually increases with cycle number. This coincides with the texture changes caused by the twinning in the compression deformation and the detwinning in the tensile deformation. Assuming that extension twinning is the only origin for texture changes, the TVF can be calculated from the variation of the ADF of the basal pole using the following equation [52]:

$$f_{twin} = \int_{\chi=0}^{\chi=50^{\circ}} \{I(\chi) - I_0(\chi)\}\ Sin\chi\ d\chi \quad (1)$$

where χ is the tilt angle between the *c*-axis and the compression direction, $I(\chi)$ is the intensity at angle χ, and $I_0(\chi)$ is the initial intensity of the twin-free condition. In the previous study, 45° and 57° were selected as the dividing points for separating the matrix and the twin orientations [48,52]. These dividing points may differ depending on the chemical composition and the initial texture. In the present study, 50° was selected as the dividing point according to which I (50°) remains constant throughout the deformation (Fig. 5a).

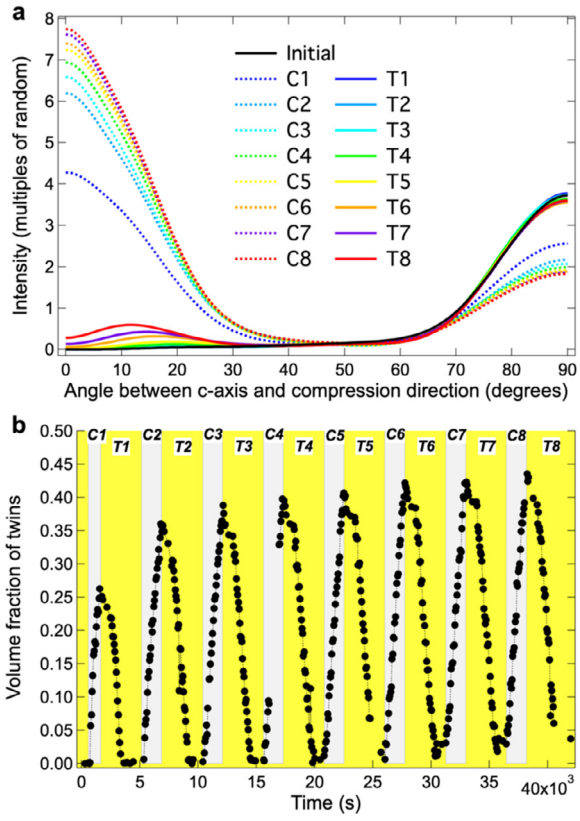

Fig. 5. (a) Axial distributions of basal poles in the sample subjected to various deformation cycles and (b) Evolution of twin volume fraction during cyclic deformation evaluated using *in-situ* neutron diffraction.

Fig. 5b shows that TVF evaluated from the ADF of the basal pole, and it increased with the compressive strain. Moreover, the TVF at the largest value of compressive strain (−2%) increased with the increase in cycle number. It was observed that the TVF of 26.3% at the first cycle increased to 43.5% at the eighth cycle. In tension, the TVF increment caused by twinning during compression was almost removed but partly remained although the tensile deformation reached the largest strain value (+2%). This indicates the presence of residual twins. Similar to the trend in TVF, the volume fraction of residual twins after each tension step increased with increasing number of cycles; that is, almost zero at the first cycle increased to 3.7% at the eighth cycle.

3.3. Detwinning behavior tracked by identical area electron backscatter diffraction

The evolutions of TVF and volume fraction of residual twins during cyclic deformation were quantitatively evaluated by *in-situ* ND, and their trends are in agreement with the qualitative results in rolled AZ31B Mg alloy [4] and extruded ZK60A [10]. The morphological details of the twins in previous studies, however, are insufficient.

Here, the identical area EBSD analysis was performed on *Sample 1* and *Sample 2* to investigate how twins introduced by different deformation histories evolve when a tensile loading is applied Fig. 6a1 and b1 shows the positions in the stress–

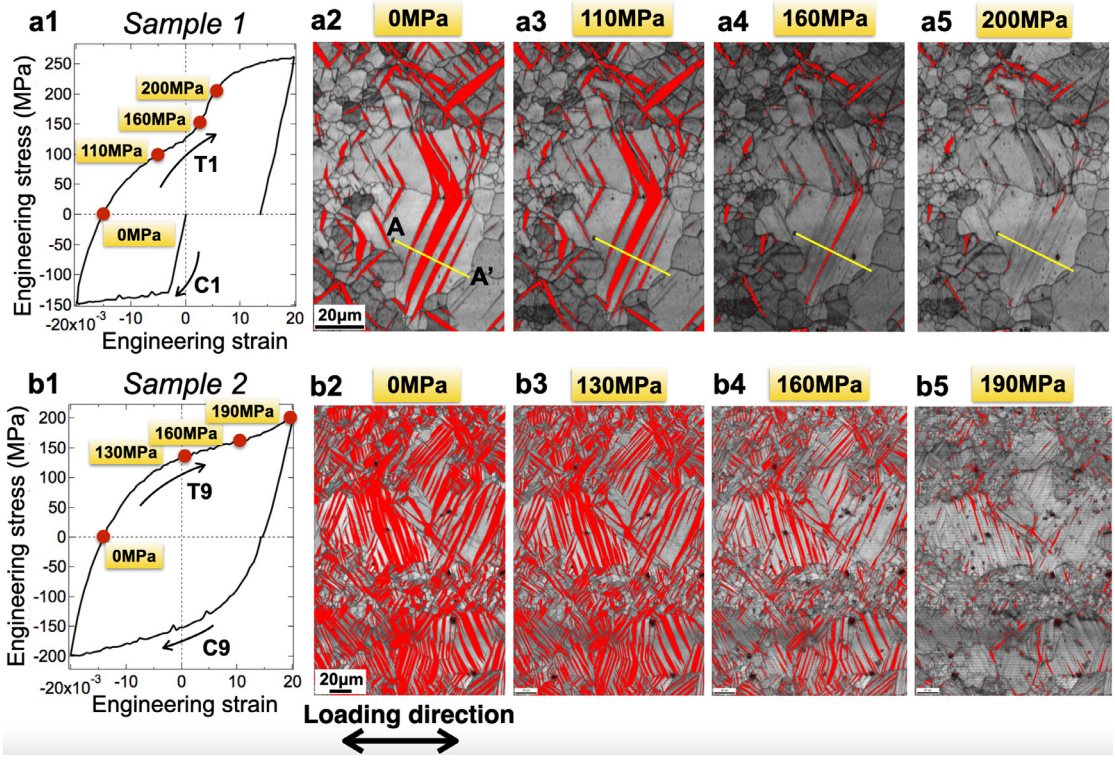

Fig. 6. Detwinning behavior during tensile deformation tracked by identical area electron backscatter diffraction analysis. (a1) Measurement positions on the stress–strain curve of the a2–a5 in *Sample 1* (−2% strained), (a2–a5) twin maps showing the microstructure evolution due to detwinning in *Sample 1*, (b1) measurement positions on the stress–strain curve of the b2–b5 in *Sample 2* (−2% strained after eight cycles of deformation), and (b2–b5) twin maps showing the microstructure evolution due to detwinning in *Sample 2*. Twins are highlighted in red (For interpretation of the references to color in this figure legend, the reader is referred to the web version of this article).

strain curves where the EBSD analses were carried out, and Fig. 6a2–a5 and b2–b5 shows the corresponding twin maps, where the twins were highlighted in red. Before tension deformation, *Sample 1* exhibited lower area fractions of twins (16.0%) than that of *Sample 2* (47.5%). Moreover, the number percentage of the grains containing twins was 20% for *Sample 1* and 44% for *Sample 2*, indicating that not only the twin fraction increased, but also additional grains were involved in twinning with increasing cycles. In the subsequent step-by-step tension, the twins gradually shrank with tensile strain in both samples Fig. 7a shows the misorientation angle distributions along the yellow lines (A–A′) in Fig. 6a2–a5. The misorientation angles of the TBs are close to 86.3°. As the deformation progresses, the twins become narrower. Basically, the narrowing of each twin was realized by the movement of one-sided TB. This needs to be verified by further studies.

Fig. 7b shows a comparison of area fractions of the twins obtained using EBSD analyses with TVF evaluated by *in-situ* ND. There are some differences, which may be related to the relatively small statistical area of the EBSD analysis. Nevertheless, it can be seen that the area fraction of twins dropped from 16.0% to 1.4% in *Sample 1* and 47.5% to 5.8% in *Sample 2* by tension. The EBSD results also confirmed the presence of residual twins similar to that evaluated using *in-situ* ND.

Despite the inhomogeneity of grain size, the texture was homogeneous in the whole sample. The average Schmid factors for $\{10\bar{1}2\}$ twinning calculated by TSL OIM software are 0.444 and 0.451 for fine and coarse grains, respectively, suggesting the equivalent favorability for twinning in crystallographic aspect Fig. 7c shows the different evolution in the area fraction of twins between coarse and fine grains. The twins were mainly observed in the coarse grains in *Sample 1* and *Sample 2*, indicating that twinning prefers to occur in the coarse grains rather than in the fine grains. This confirms the findings of many studies on the grain size dependence of deformation twinning [12,19,20,53,54]. In *Sample 2*, additional fine grains were also involved in twinning, suggesting that cyclic compressive–tensile deformation promoted the twinning activity in fine grains Fig. 7d shows that the decrement rates of the area fraction of twins in coarse and fine grains were almost similar with each other in the same sample. As we know, twinning can generally be divided into two steps, namely, twin initiation and twin growth through moving TBs. Detwinning is similar to the process of grain growth, but the TBs move in the opposite direction to shrink the twins [42,55]. The EBSD results indicate that twinning had a grain size effect, while detwinning exhibited a weak sensitivity to the grain size. It may be understood that the grain size has a significant effect on twin initiation but hardly affects the

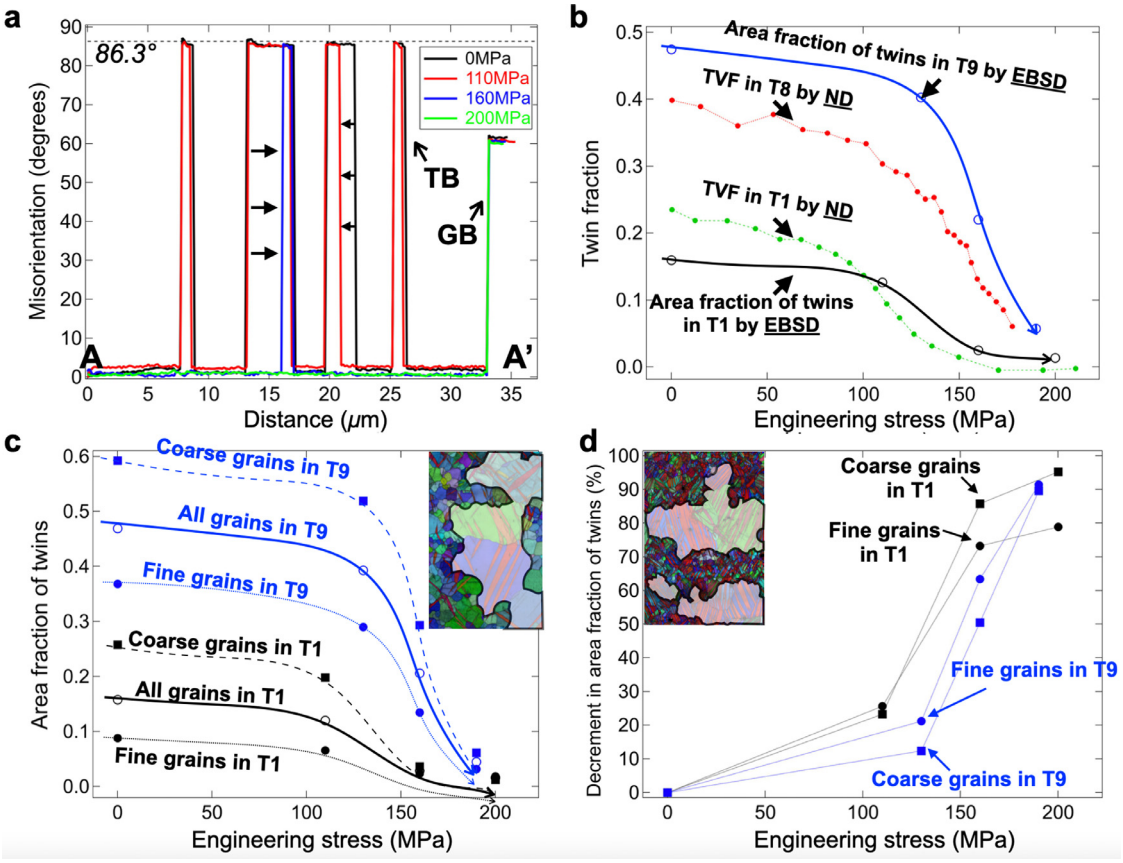

Fig. 7. (a) Profiles present misorientation angles relative to the orientations along A–A′ lines in Fig. 6a2–a5 showing the motion of twin boundaries due to detwinning, (b) comparison of area fraction of twins with volume fraction of twins evaluated using electron backscatter diffraction and neutron diffraction, respectively. Comparison of (c) evolution of area fraction of twins and (d) corresponding decrement caused by tensile deformation between coarse and fine grains. The coarse grains (highlight) and fine grains (without highlight) of *Sample 1* and *Sample 2* for evaluation are shown in the inset of (c) and (d).

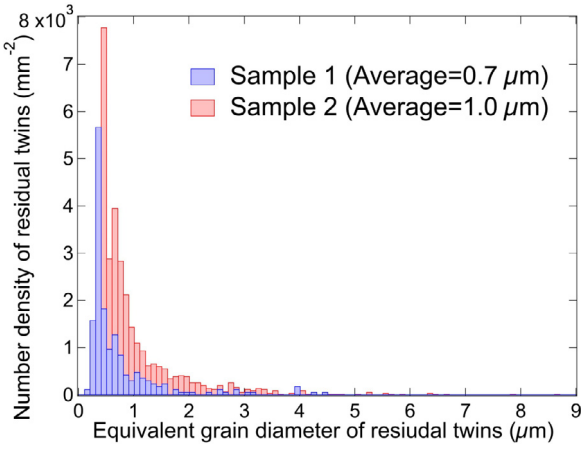

Fig. 8. Comparison of grain size distributions of residual twins between *Sample 1* and *Sample 2* after tension.

movement of TBs, because the latter occurs inside the grains and results in less interaction with grain boundaries.

Fig. 8 shows the number of residual twins as a function of their equivalent grain diameter in *Sample 1* and *Sample 2* after tension. As the number of cycles increased from *T1* to *T9*, the equivalent grain diameter of the residual twins became slightly coarser (average grain size: 0.7 μm → 1.0 μm) and the number density (number/indexed area) of residual twins increased significantly (1.60×10^4 mm^{-2} → 3.15×10^4 mm^{-2}).

Fig. 9 presents the boundary maps and Kernel average misorientation (KAM) maps to express the changes in boundary density and dislocation density with cyclic deformation, respectively. The boundary maps of *Sample 1* and *Sample 2*, including low angle grain boundaries (LAGBs: 2°∼15°), high angle grain boundaries (HAGBs: >15°), and $\{10\bar{1}2\}$ twin boundaries (TBs: 86.3°± 5°) combined with the $\{10\bar{1}2\}$ twins highlighted in red, are shown in Fig. 9a and b, respectively. Considerably more TBs in *Sample 2* than *Sample 1* can be observed. The LAGBs mainly distributed in twins (see inset of Fig. 9b) similar to the previous study [8,30]. The quantitative comparison of various boundaries was expressed by boundary density (length of boundary/indexed area) in Fig. 9c. The sample before deformation (i.e., *Sample 0*) was added for reference. As seen, the boundary densities of all boundaries (LAGBs + HAGBs) are 350 mm^{-1}, 861 mm^{-1}, and 1205 mm^{-1} for *Sample 0, Sample 1*, and *Sample 3*, showing a remarkably increasing tendency with increasing number of cycles. The increment in boundary density of all the boundaries is mainly contributed by those of TBs (0 mm^{-1} → 345 mm^{-1} → 509 mm^{-1}) and LAGBs

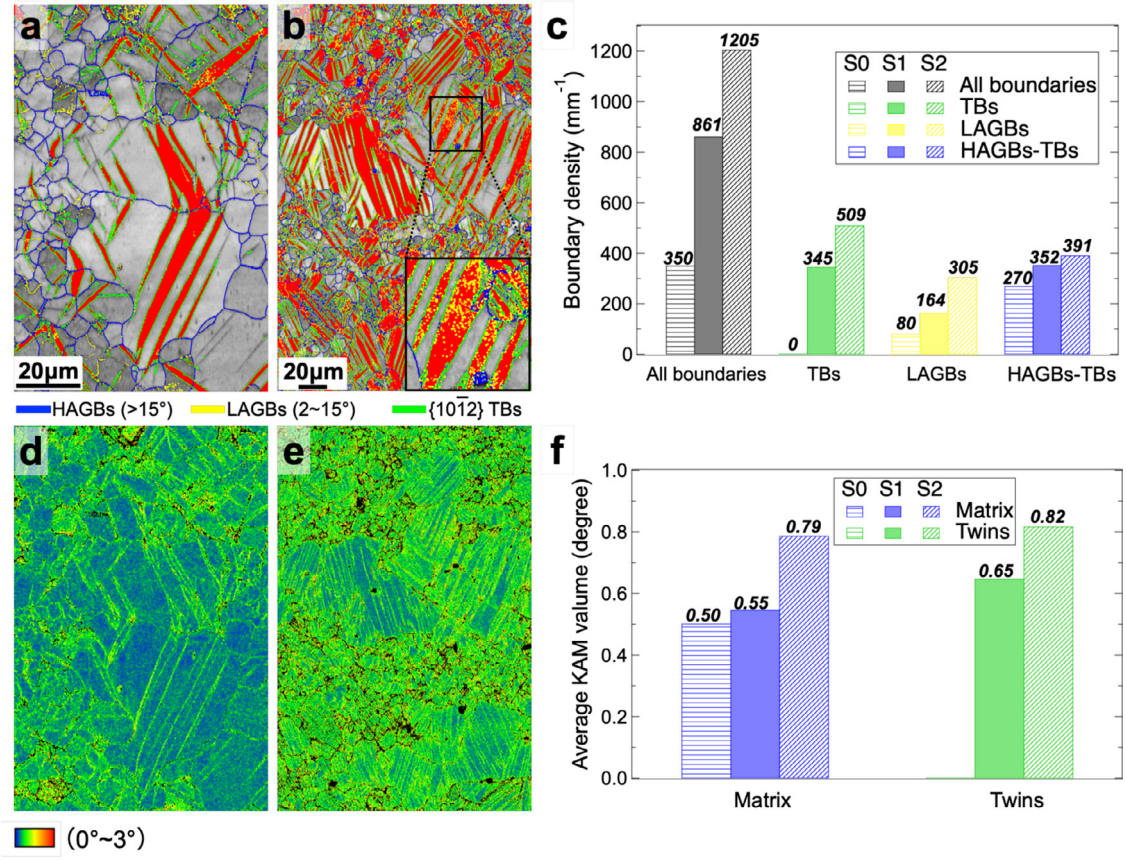

Fig. 9. Grain boundaries on image quality maps of (a) *Sample 1* and (b) *Sample 2* showing low angle grain boundaries (LAGBs), high angle grain boundaries (HAGBs), and {10$\bar{1}$2} twin boundaries (TBs: 86.3°±5°), and (c) the corresponding changes in boundary density after different cycles (S0, S1, and S2 refer to *Sample 0, Sample 1*, and *Sample 2*). The inset in (b) enlarged the frame area to show the distribution of LAGBs. KAM maps of (d) *Sample 1* and (e) *Sample 2*, and (c) the corresponding changes in average KAM value of matrix and twins after different cycles (For interpretation of the references to color in this figure, the reader is referred to the web version of this article).

(80 mm^{-1} → 164 mm^{-1} → 305 mm^{-1}). Interestingly, the HAGBs with excluding the TBs also exhibited a slight increase with increasing cycles, which may be contributed by the twin-twin boundaries or LAGBs to HAGBs transition Fig. 9d and e show the KAM maps of *Sample 1* and *Sample 2*, respectively. The KAM value, as a parameter representing the dislocation density, is obviously higher in *Sample 2* than that of *Sample 1*. The average KAM values of matrix and twins were separated and compared in Fig. 9f. The KAM value of matrix increased slightly (0.5 ° → 0.55 °) after $a - 2\%$ compressive strain, and then increased to 0.79 ° in *Sample 2*. The KAM values of twins exhibited a similar tendency to that of matrix, but were consistently higher than the latter. In brief, the cyclic deformation introduced various barriers including TBs, LAGBs, and dislocations in matrix and twins. Combined with the volume fraction and number density of residual twins described above, these microstructure parameters are crucial to influence the mechanical responses.

3.4. Mechanical responses in cyclic deformation

The stress–strain curves of the cyclic compressive–tensile deformation shown in Fig. 10a demonstrate a strong asymmetry between compression and tension, which is quite similar to those typically found in wrought Mg alloys [4,10]. In the first compression stage, there was a plateau with weak work hardening after yielding. Such a plateau is a typical mechanical response when {10$\bar{1}$2} twinning is dominant in textured Mg alloys [13,48]. The plateau was caused by the avalanche-like formation of twinning [13]. A pseudo-elastic behavior that appeared during unloading after compression is frequently associated with the detwinning driven by the intergranular stress [11,13]. In the subsequent tensile deformation, the stress–strain relationship shows a curved shape that continues from the unloading after compression without a linear elastic region. It can be considered that the occurrence of detwinning accommodating strain resulted in the absence of an elastic region in the tension stage. When the absolute strain in tension exceeded zero strain, an inflection point that was followed with a work hardening stage appeared. This inflection point is considered to be a transition from detwinning dominant deformation to dislocation slip dominant deformation. Note that there are some stress drops in the stress-strain curves, which are the products of strain gage control method. Because when the twins formed at the surface where the strain gage attached, a sudden increase in strain led to a rapid decrease in crosshead speed, and then resulted in a stress drop in stress strain curve.

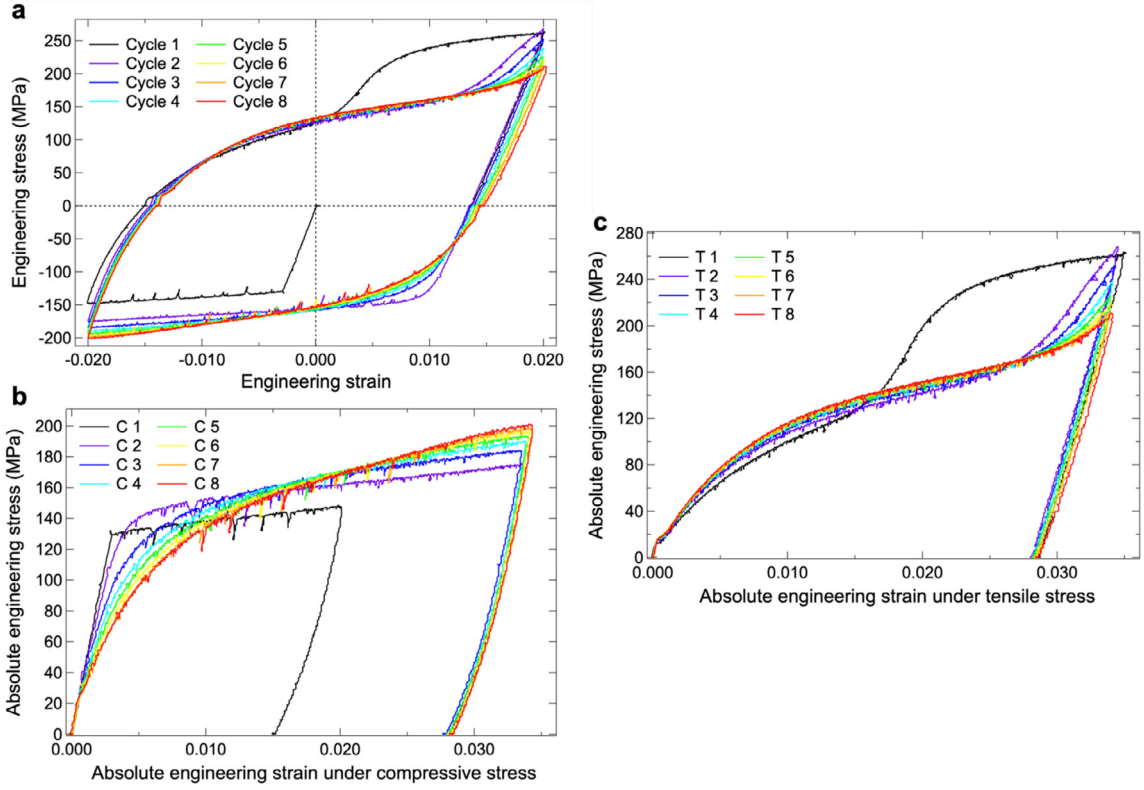

Fig. 10. Stress–strain curves in cyclic deformation. (a) Engineering stress–strain curves of cyclic deformation showing a strong asymmetry between compression and tension, (b) stress–strain curves of compression, and (c) stress–strain curves of tension.

For simplicity, the stress–strain curves were separated into a compressive stress part in Fig. 10b and a tensile stress part in Fig. 10c. In Fig. 10b and c, stress and strain values of compression curves were plotted in positive values, and the strain values at unloaded conditions were shifted to zero. With increasing the loading cycles, the stress–strain curves in compression and tension evolved as follows:

- In compression, the yield strength defined by the deviation from the linear elastic response decreased gradually, but in the following plastic deformation, the work hardening rate increased gradually, resulting in an increase in the absolute peak stress at the largest compressive strain.
- In tension, the stress increased at the beginning of deformation, but the inflection point of the slope of the work hardening gradually shifted to a high strain level, resulting in a decrease in the peak stress at the largest tensile strain.

3.5. Interaction between dislocations and twin boundaries

In the present study, plastic deformation was dominated by twinning and detwinning through the motions of TBs, and accommodated partly by dislocation movement. Therefore, the interactions between dislocation and TBs may play a crucial role in controlling the plastic deformation behavior. In this section, special attention was focused on the interactions between the dislocations and the TBs, and the relevant results obtained by TEM analysis were summarized.

Sample 1 with abundant $\{10\bar{1}2\}$ twins introduced by $a-2\%$ compressive strain was selected for TEM analysis Fig. 11a shows the microstructure of a typical grain containing a deformation twin. The compression direction (i.e., the ED) is almost parallel to the horizontal direction. According to the selected area electron diffraction (SAED) patterns (Fig. 11b–d), the matrix, twinned, and detwinned regions were determined and labeled in Fig. 11a. The SAED patterns in Fig. 11b and c show that the matrix and twins share the common zone axis (ZA) of $< 11\bar{2}0 >$ but their c-axes are oriented approximately perpendicular to each other. An accurate crystallographic orientation relationship between matrix and twin was determined from the SAED pattern obtained at the matrix/twin interface (Fig. 11d). The matrix and twins shared a common ZA $< 11\bar{2}0 >$, a common $\{10\bar{1}2\}$ (i.e., the twin plane), and a deviation of 86.3° between their c-axes. The crystallographic orientation relationship is consistent with the classic $\{10\bar{1}2\}$ twin mode (Fig. 11e), although recent studies have reported that the basal planes of the matrix and twin have a perpendicular relationship in a single crystal of Mg [56].

Under the diffraction condition that ZA is parallel to $< 11\bar{2}0 >$ of both matrix and twin as illustrated by Fig. 11e, abundant straight dislocations are visible in both matrix and twin (Fig. 11a). Most of the dislocations are aligned parallel

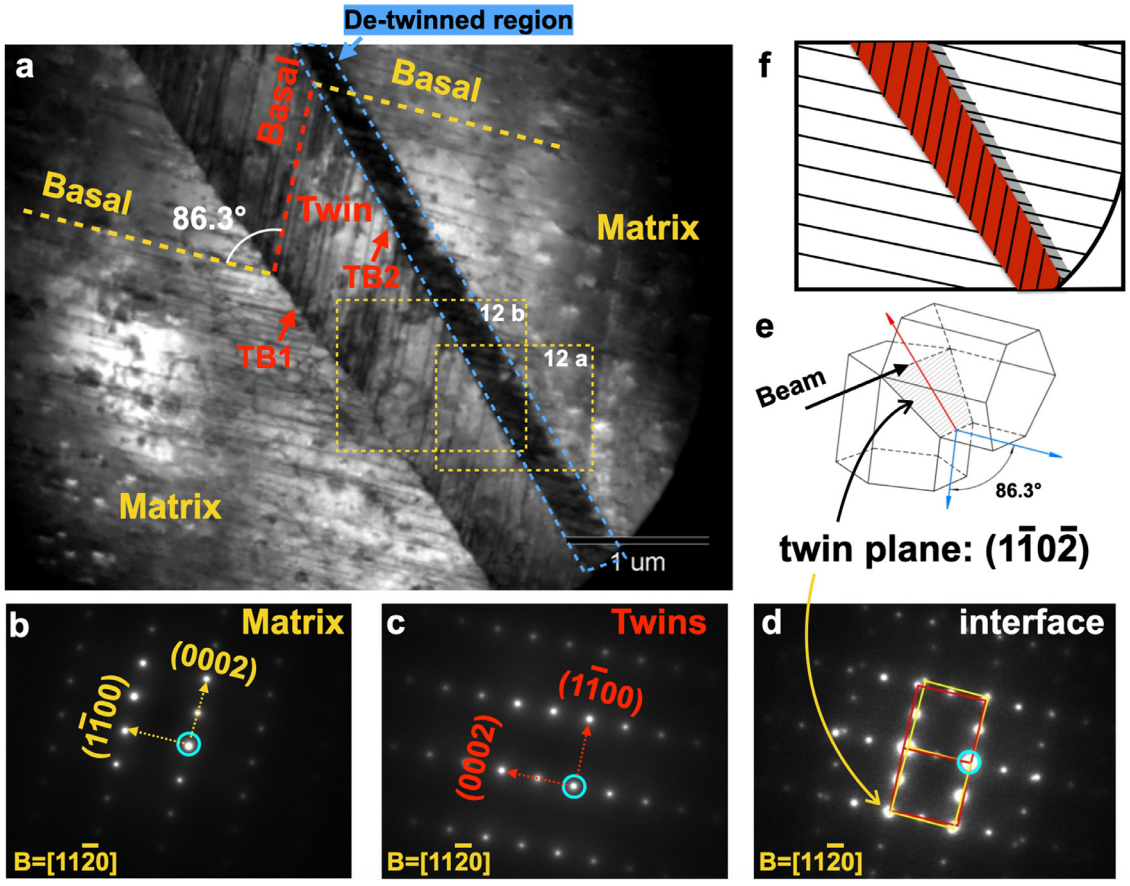

Fig. 11. (a) Transmission electron microscopy image showing straight dislocations within the matrix and the twin parallel to basal plane traces. SAED patterns of (b) matrix, (c) twin, and (d) both the matrix and the twin on < 11$\bar{2}$0 > ZA. (e) Schematic illustration showing orientation relationship of {10$\bar{1}$2} twinning. (f) Schematic illustration showing dislocation distributions in the matrix, twin, and the detwinned region. TB1 and TB2 mean the twin boundaries.

to the basal planes in both the matrix and twin; therefore, they are likely to be the basal dislocations.

Because the incident beam was parallel to the twin plane, the matrix/twin interface should be narrow under this observation condition. As can be seen, only the lower left side of the interface (see TB1 in Fig. 11a) was observed clearly, but a dark band exists between the twin and matrix on the higher right side of the interface (near TB2 in Fig. 11a). By comparing the SAED patterns between the dark band region and the adjacent matrix, it was found that they had almost the same orientation with a misorientation angle of approximately 1.5° As mentioned above, detwinning already started during unloading in compression. The dark band is considered as the detwinned region, and a similar morphology of the detwinned region was also observed using EBSD (Fig. 6). The dislocations in the detwinned region are highly dense and have a straight shape being parallel to the basal plane of the matrix. According to the results shown in Fig. 11a and a schematic drawn in Fig. 11f, the dislocations in the matrix, twinned, and detwinned regions show differences in orientation and density.

The well-known "$g \bullet b = 0''$ invisibility criterion (where g and b are the diffraction vector and the Burgers vector, respectively) was used to distinguish the types of dislocations Fig. 12a shows a TEM image when the specimen was tilted to a two-beam condition with $g = 0002$ reflection of the matrix. Under this diffraction condition, the <a> dislocations with $b = 1/3 < 11\bar{2}0 >$ are invisible. In contrast, the dislocations with <c>-component in the Burgers vector have good contrast for this condition. As can be seen, the matrix part is blank, suggesting that the dislocations in the matrix observed in Fig. 11a are <a> dislocations. Interestingly, abundant dislocations are visible in the detwinned region, indicating that these dislocations have a <c>-component in the Burgers vector. In the same way, a strong diffraction contrast from the <c>-component can be observed in the twinned region under $g = 0002$ reflection in twins (Fig. 12b).

4. Discussion

4.1. Formation of <c>-component dislocations during twinning and detwinning

<c>-component dislocations in Mg alloys are generated base on two independent mechanisms. One is pyramidal slip [5,57,58] and the other is dislocation transmutation. The so-called dislocation transmutation during twinning was reported in various HCP metals such as Mg and Zr [31–33,35,59]. When the <a> dislocations introduced by a basal slip or pris-

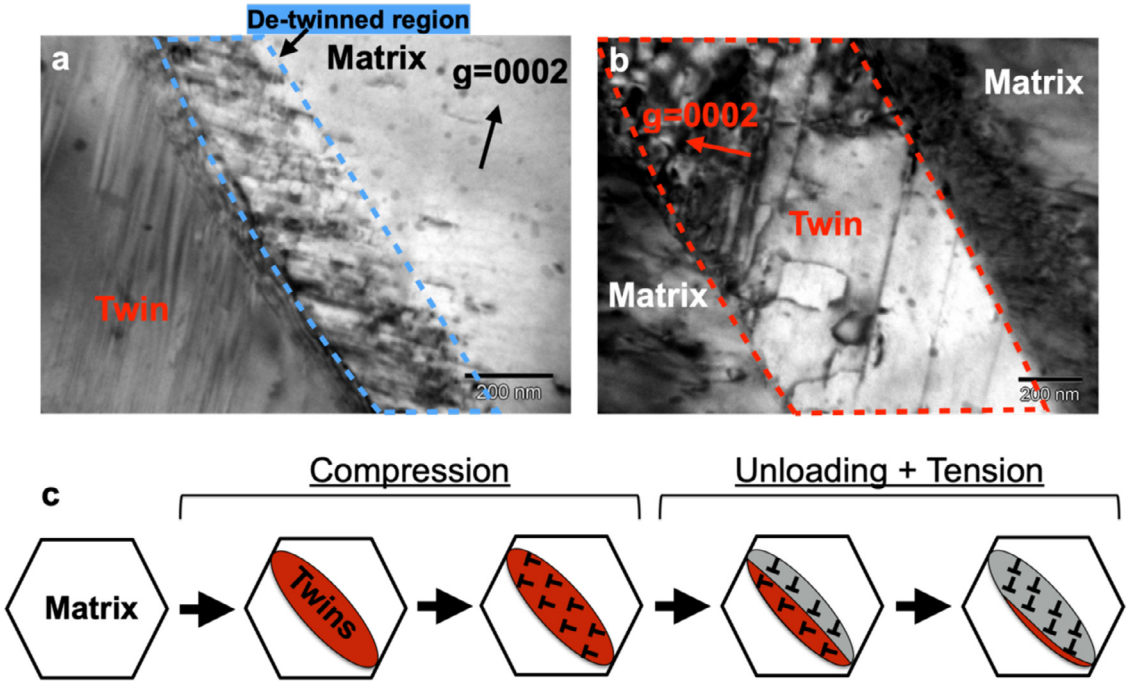

Fig. 12. Dislocation transmutation. (a) Bright-field image of the matrix with $g = 0002$ showing dislocations having <c>-component Burgers vector in the detwinned region, (b) bright-field image of the twin with $g = 0002$ showing dislocations having <c>-component Burgers vector within the twin, and (c) schematic illustration showing the generation of <c>-component Burgers vector dislocations in the detwinned region. The observation areas of (a) and (b) are the rectangles shown in Fig. 11a.

matic slip in the matrix of Mg or Zr penetrate to the $\{10\bar{1}2\}$ TBs, the Burgers vector of <a> in the matrix will be transformed into <c + a> or <a> in twins. Moreover, abundant stacking faults lying in the basal planes of twins have been frequently observed in various hcp metals such as Be [60], Zr [59,61], Ti [61], and Mg [36,37]. Recently, these stacking faults in Mg have been determined to be the I_1 stacking faults formed by glissile-to-sessile transition during twinning analogous to the Basinski mechanism [36,37]. Therefore, the present observed <c>-component dislocations aligned parallel to the basal planes in twins are possibly sessile partial dislocations of I_1 stacking faults formed by the reaction between the basal dislocations and TBs.

Considering that the basal plane of the matrix in Fig. 11a was not completely parallel to the compression direction and then the Schmid factor for basal slip cannot be neglected. Undoubtedly, the straight <a> dislocations lying in the basal plane in the matrix were introduced by a basal slip at an early stage of compressive deformation. The dislocations in twins with <c>-component also lying in the basal plane may inherit from the <a> dislocations in the matrix through dislocation transmutation. With further compressive deformation, <a> dislocations may also be introduced in twins by basal slip [3].

Detwinning is similar to twin growth, both of which are completed through motion of TBs but in opposite directions. Therefore, the dislocation transmutation that occurred during twinning may also occur during detwinning. When <a> dislocations were introduced in twins by basal slip during compressive deformation, these dislocations had a chance to be transmuted into <c>-component dislocations during detwinning, as that occurred during twinning. It has been reported that basal slip can be active in twins [3], and the basal slip was feasible in the twins observed in Fig. 11 because its basal plane-normal were not parallel to the loading direction. In brief, the generation of <c>-component dislocations in the detwinned region can be comprehended by the illustration in Fig. 12c. First, the $\{10\bar{1}2\}$ twins formed in the matrix under the compressive deformation, then the <a> dislocations were introduced by basal slips in twins when the resolved shear stress applied on the basal plane exceeded the CRSS. In the subsequent unloading and tension stages, detwinning occurred to shrink the twins, and interactions between the dislocations in twins and the motion of TBs led to the dislocation transmutation. As a result, dislocations with <c>-component remained in the detwinned region.

4.2. Mechanical response and microstructure evolution during cyclic deformation

The present material has a strong extrusion texture. This condition favors extensive $\{10\bar{1}2\}$ twinning in compressive deformation and detwinning in subsequent tensile deformation [4,10]. The evolutions of twinning and detwinning play key roles during cyclic loading deformation. Here, the stress–strain curves and variations of the TVF of the second and seventh cycles were picked up as shown in Fig. 13a and b for discussion.

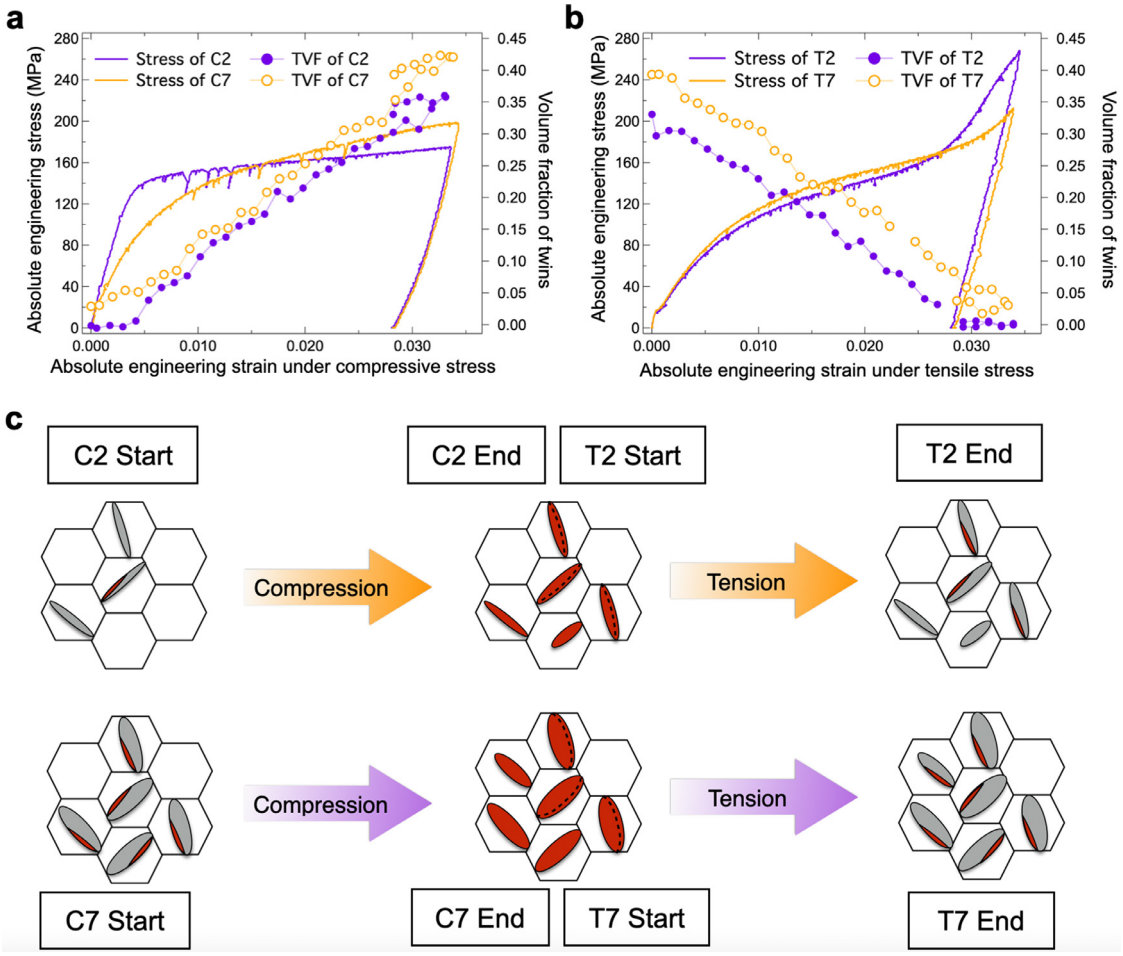

Fig. 13. Relationship between deformation mechanisms and stress–strain behavior. Comparison of stress–strain curves and variations of the twin volume fraction between the second and seventh cycles in (a) compression and (b) tension, respectively. (c) Schematic showing the comparison of twinning and detwinning behavior in the second and seventh cycles.

In *C2*, an apparent elastic region with a linear relationship between the stress and strain can be observed, but not in *C7*. Correspondingly, an increase in the TVF was observed from the beginning of *C7*. The early yielding may be attributed to the growth of residual twins because the CRSS for twin growth is significantly lower than that for twin initiation [4,55]. As illustrated in Fig. 13c, the fraction of residual twins in the sample before *C7* is higher and distributed in more grains than that before *C2*, which can be predicted from the EBSD results shown in Fig. 6. As has been reviewed systematically, numerous studies related to the effect of pre-strain on twinning and detwinning behavior have been conducted in recent years [62], and they concluded that the twin boundary mobility associated with mechanical properties depends on the size of twins and dislocation density in the pre-strained sample [27–29]. Small twins with less dislocations introduced by a light pre-strain showed an improvement on twin boundary mobility, whereas a heavy pre-strain suppressed the motion of twin boundary significantly due to the high dislocation density [27]. Here, the higher KAM value in twins than that in matrix may lead the twin shrinkage more difficult than twin growth, and then resulted in more residual twins with increasing number of cycles. The residual twins provide sufficient sites for accommodating the strain via twin growth, and thus reduces the yield strength. In the subsequent plastic compressive deformation, the increasing rates of TVF with the strain became nearly linear (Fig. 13a). The higher fraction of initial residual twins and early yielding led to a higher fraction of twins at the end of *C7* than that of *C2*.

The stress–strain curve indicates that *C7* exhibits higher work hardening behavior than that of *C2*, resulting in higher stress at the end of compression. As supported by the EBSD analysis (Fig. 9), various barriers were introduced in microstructure during cyclic deformation, which are considered to be the reasons for the enhanced work hardening with increasing number of cycles as follows:

- The accumulation of dislocations in matrix and twins;
- An increase in the number of TBs and dislocation density in the matrix enhanced the interactions between the TBs and dislocations;
- The twinning spreading from coarse grains toward fine grains increased the interactions between the grain boundaries and the TBs.

The stress–strain curves of *T2* and *T7* in tension shown in Fig. 13b demonstrate a similar shape in the detwinning dominant stage where the linear relations between the stress and strain were not observed from the beginning of tensile deformation. According to the evolution of TVF, the stress-strain curve can be subdivided into two regimes. For strain region of $0 \sim 0.027$ (regime 1), TVF decreased linearly with strain indicating the detwinning-dominated regime. For strain > 0.027 (regime 2), the decrease rate of TVF slows down and to saturate indicating the exhaustion of detwinning. As described above, more grains were involved in twinning at *C7* than at *C2*. In regime 1, the twinned regions being favorable for detwinning act like soft grains in comparison with the twin-free grains. Accordingly, stresses during the detwinning stage at *T7* are expected to be lower than at *T2*, due to the increase in TVF with increasing cycles. However, the stress–strain curves exhibited an opposite behavior, where the stress in regime 1 at *T7* is higher than that at *T2* (Fig. 13b). This implies that significant work hardening is accompanied by detwinning. To interpret this, we focused on the shrinkage of twins and the barriers in twins. Numerous LAGBs are observed in twins and their boundary density as well as the KAM value increased with cycle number. The LAGBs (i.e., dislocation walls) and dislocations in twins can serve as barriers to suppress the motion of TBs.

As revealed by TEM observation shown in Fig. 12, abundant dislocations with <c>-component in the twinned region and detwinned region generated by dislocation transmutation during twinning and detwinning were confirmed. The cyclic deformation not only increased the number of TB and dislocation density but also increased the degree of dislocation multiplicity, i.e., dislocation type. Kadiri and Oppedal [31] and Oppedal et al [32]. have reported that the dislocation multiplicity can provide extra hardening through modeling studies. Liu et al [63]. conducted *in-situ* TEM observation on Mg single crystal during tension-compression cyclic deformation and found that the stress for detwinning was higher than that of twinning. More types of defects in twins than that in matrix could be responsible to the observed twinning-detwinning asymmetry. Here, the increase in TBs and dislocation density and multiplicity led to the enhanced interaction between dislocations and motion of TBs, and this is considered to increase the stress during the detwinning stage in regime 1.

In regime 2, there is no deformation mode accommodating the strain due to the exhaustion of detwinning, and then the stress-strain curve behaves more elastically. The reduced peak stress at the largest tensile strain in a large number of cycles was due to larger strain needed for detwinning a larger amount of twinned region, which squeezed the strain of regime 2 for elastic strain hardening.

From the above discussion, the activities of twinning and detwinning during cyclic deformation are closely related to the microstructure parameters including grains size and dislocation structures. Moreover, the favorability of twinning and detwinning is also strongly depended on the crystallographic orientation of the grains, but was not deeply discussed in present work and will be investigated and reported in the near future.

5. Conclusions

In summary, *in-situ* ND, identical area EBSD, and TEM techniques were employed to systematically evaluate the cyclic compression–tension deformation behavior of the extruded AZ31 alloy. The specific conclusions are as follows:

(1) The compressive deformation was dominated by twinning. Detwinning occurred during unloading after compression and dominated the tensile deformation. A basal slip was also activated in both the matrix and twins.
(2) With increasing number of cycles, the TVF at −2% strain gradually increased from 26.3% (1st cycle) to 43.5% (8th cycle). Meanwhile, the twinning spread from coarse grains to fine grains involving more grains for twinning.
(3) The lattice defects including TBs, LAGBs and dislocations were introduced by cyclic deformation and their densities increased with cyclic number.
(4) After the tension step, the volume fraction and number of residual twins increased with cycle number, which led to the decrease in yield stress in the subsequent compression.
(5) Dense <c>-component dislocations observed in twins and matrices near the TBs were generated by the dislocation transmutation during twinning and detwinning, respectively.
(6) The accumulation of dislocations and the increase in the number of TBs did not contribute to work hardening independently, but through the interaction between them during twinning and detwinning to enhance the work hardening, which is believed to play a crucial role in cyclic deformation of the commercial AZ31 alloy.

Acknowledgments

This work was financially supported by the Elements Strategy Initiative for Structural Materials (ESISM, grant No. JPMXP0112101000) in Kyoto University. RXZ was supported by National Natural Science Foundation of China (NSFC, No. 51901007). SH and KA were supported by JSPS KAKENHI Nos. JP18H05479 and JP18H05476. The neutron diffraction experiments at the Materials and Life Science Experimental Facility of the J-PARC were performed under a project program (Project No. 2014P0102).

References

[1] M.H. Yoo, Metal. Trans. A 12 (1981) 409–418.
[2] J.W. Christian, S. Mahajan, Prog. Mater. Sci. 39 (1995) 1–157.
[3] M.R. Barnett, Mater. Sci. Eng. A 464 (2007) 1–7.
[4] X.Y. Lou, M. Li, R.K. Boger, S.R. Agnew, R.H. Wagoner, Int. J. Plast. 23 (2007) 44–86.
[5] S.R. Agnew, M.H. Yoo, C.N. Tomé, Acta Mater. 49 (2001) 4277–4289.
[6] J. Koike, Metall. Mater. Trans. A 36 (2005) 1689–1696.

[7] J. Čapek, K. Máthis, B. Clausen, M. Barnett, Acta Mater. 130 (2017) 319–328.
[8] Y. Cui, Y. Li, Z. Wang, X. Ding, Y. Koizumi, H. Bian, L. Lin, A. Chiba, Int. J. Plast. 91 (2017) 134–159.
[9] Y.N. Wang, J.C. Huang, Acta Mater. 55 (3) (2007) 897–905.
[10] L. Wu, A. Jain, D.W. Brown, G.M. Stoica, S.R. Agnew, B. Clausen, D.E. Fielden, P.K. Liaw, Acta Mater. 56 (4) (2008) 688–695.
[11] L. Wu, S.R. Agnew, D.W. Brown, G.M. Stoica, B. Clausen, A. Jain, D.E. Fielden, P.K. Liaw, Acta Mater. 56 (2008) 3699–3707.
[12] D. Drozdenko, J. Bohlen, S. Yi, P. Minárik, F. Chmelík, P. Dobroň, Acta Mater. 110 (2016) 103–113.
[13] O. Muránsky, D.G. Carr, P. Šittner, E.C. Oliver, Int. J. Plast. 25 (6) (2009) 1107–1127.
[14] M.A. Gharghouri, G.C. Weatherly, J.D. Embury, J. Root, Philos. Mag. A 79 (1999) 1671–1695.
[15] W. Tang, J.Y. Lee, H. Wang, D. Steglich, D. Li, Y. Peng, P. Wu, J. Magnes. Alloy. 9 (2021) (2021) 927–936.
[16] N. Tsuji, Y. Ito, Y. Saito, Y. Minamino, Scr. Mater. 47 (2002) 893–899.
[17] K.S. Kumar, H. Van Swygenhoven, S. Suresh, Acta Mater. 51 (19) (2003) 5743–5774.
[18] K. Lu, L. Lu, S. Suresh, Science 324 (2009) 349–352.
[19] M.R. Barnett, Scr. Mater. 59 (2008) 696–698.
[20] R. Zheng, T. Bhattacharjee, S. Gao, W. Gong, A. Shibata, T. Sasaki, K. Hono, N. Tsuji, Sci. Rep. 9 (2019) 1–14.
[21] N. Hansen, R.F. Mehl, Metall. Mater. Trans. A 32 (2001) 2917–2935.
[22] A. El-Azab, Science 320 (2008) 1729–1730.
[23] I. Tamura, Met. Sci. 16 (1982) 245–253.
[24] L. Lu, X. Chen, X. Huang, K. Lu, Science 323 (2009) 607–610.
[25] J.F. Nie, Y.M. Zhu, J.Z. Liu, X.Y. Fang, Science 340 (2013) 957–960.
[26] Y. Wei, Y. Li, L. Zhu, Y. Liu, X. Lei, G. Wang, Y.X. Wu, J.B. Z.M, H. Wang, H. Gao, Nat. Commun. 5 (2014) 3580 3580.
[27] Y. Cui, H. Bian, Y. Li, Y. Zhao, K. Aoyagi, A. Chiba, J. Alloy. Compd. 816 (2020) 152496.
[28] D. Sarker, J. Friedman, D.L. Chen, Mater. Sci. Eng. A 605 (2014) 73–79.
[29] Q. Wang, B. Jiang, J. Zhao, D. Zhang, G. Huang, F. Pan, Mater. Sci. Eng. A 798 (2020) 140069.
[30] Y. Xin, L. Lv, H. Chen, C. He, H. Yu, Q. Liu, Mater. Sci. Eng. A 662 (2016) 95–99.
[31] H. El Kadiri, A. Oppedal, J. Mech. Phys. Solids 58 (2010) 613–624 27.
[32] A.L. Oppedal, H. El Kadiri, C.N. Tomé, G.C. Kaschner, S.C. Vogel, J.C. Baird, M.F. Horstemeyer, Int. J. Plast. 30-31 (2012) 41–61 28.
[33] F. Wang, S.R. Agnew, Int. J. Plast. 81 (2016) 63–86 29.
[34] K.D. Molodov, T. Al-Samman, D.A. Molodov, Acta Mater. 124 (2017) 397–409 30.
[35] S. Morozumi, M. Kikuchi, H. Yoshinaga, Trans. JIM 17 (1976) 158–164 31.
[36] F. Wang, K. Hazeli, K.D. Molodov, C.D. Barrett, T. Al-Samman, D.A. Molodov, A. Kontsos, K.T. Ramesh, H. El Kadiri, S.R. Agnew, Scr. Mater. 143 (2018) 81–85.
[37] F. Wang, C.D. Barrett, R.J. McCabe, H. El Kadiri, L. Capolungo, S.R. Agnew, Acta Mater. 165 (2019) 471–485.
[38] M. Niewczas, Acta Mater. 58 (2010) 5848–5857 32.
[39] W. Gong, K. Aizawa, S. Harjo, R. Zheng, T. Kawasaki, J. Abe, T. Kamiyama, N. Tsuji, Int. J. Plast. 111 (2018) 288–306 33.
[40] S. Harjo, K. Aizawa, W. Gong, T. Kawasaki, Mater. Trans. 61 (2020) 828–832 34.
[41] M.A. Kumar, I.J. Beyerlein, R.J. McCabe, C.N. Tomé, Nat. Commun. 7 (2016) 13826 35.
[42] Y. Zhu, D. Hou, Q. Li, J. Magnes. Alloy. (2021), doi:10.1016/j.jma.2021.08.025.
[43] S.H. Park, S.G. Hong, C.S. Lee, Mater. Sci. Eng. A 570 (2013) 149–163 37.
[44] S. Harjo, T. Ito, K. Aizawa, H. Arima, J. Abe, A. Moriai, T. Iwahashi, T. Kamiyama, Mater. Sci. Forum 681 (2011) 443–448 38.
[45] R. Oishi Tomiyasu, M. Yonemura, T. Morishima, A. Hoshikawa, S. Torii, T. Ishigaki, T. Kamiyama, J. Appl. Crystallogr. 45 (2012) 299–308 39.
[46] L.S. Lutterotti, S. Matthies, H.R. Wenk, IUCr-CPD Newslett. 21 (1999) 14 40.
[47] R. Hielscher, H. Schaeben, J. Appl. Crystallogr. 41 (2008) 1024–1037 41.
[48] B. Clausen, C.N. Tomé, D.W. Brown, S.R. Agnew, Acta Mater. 56 (2008) 2456–2468 42.
[49] H. Ding, L. Liu, S. Kamado, W. Ding, Y. Kojima, J. Alloys Compd. 456 (2008) 400–406.
[50] S.H. Park, S.H. Kim, Y.M. Kim, B.S. You, J. Alloy. Compd. 646 (2015) 932–936.
[51] D. Guan, W.M. Rainforth, J. Gao, J. Sharp, B. Wynne, L. Ma, Acta Mater. 135 (2017) 14–24.
[52] S.R. Agnew, R.P. Mulay, F.J. Polesak Iii, C.A. Calhoun, J.J. Bhattacharyya, B. Clausen, Acta Mater. 61 (10) (2013) 3769–3780 43.
[53] Q. Yu, Z.W. Shan, J. Li, X. Huang, L. Xiao, J. Sun, E. Ma, Nature 463 (2010) 335–338 44.
[54] I.J. Beyerlein, L. Capolungo, P.E. Marshall, R.J. McCabe, C.N. Tomé, Philos. Mag. A 90 (2010) 2161–2190 45.
[55] H. Qiao, S.R. Agnew, P.D. Wu, Int. J. Plast. 65 (2015) 61–84 46.
[56] B.Y. Liu, J. Wang, B. Li, L. Lu, X.Y. Zhang, Z.W. Shan, J. Li, C.L. Jia, J. Sun, E. Ma, Nat. Commun. 5 (2014) 4297 47.
[57] T. Obara, H. Yoshinga, S. Morozumi, Acta Metall. 21 (1973) 845–853 48.
[58] S.R. Agnew, J.A. Horton, M.H. Yoo, Metall. Mater. Trans. A 33 (2002) 851–858 49.
[59] D. Bhattacharyya, E.K. Cerreta, R. McCabe, M. Niewczas, G.T. Gray, A. Misra, C.N. Tomé, Acta Mater. 57 (2009) 305–315 50.
[60] J.P. Poirier, J. Antolin, J.M. Dupouy, Canad. J. Physics 45 (2) (1967) 1221–1224.
[61] S.G. Song, G.T. Gray, Philos. Mag. A 71 (1995) 263–274.
[62] T. Liu, Q. Yang, N. Guo, Y. Lu, B. Song, J. Magnes. Alloy. 8 (2020) 66–77.
[63] B.Y. Liu, K.E. Prasad, N. Yang, F. Liu, Z.W. Shan, Acta Mater. 179 (2019) 414–423.